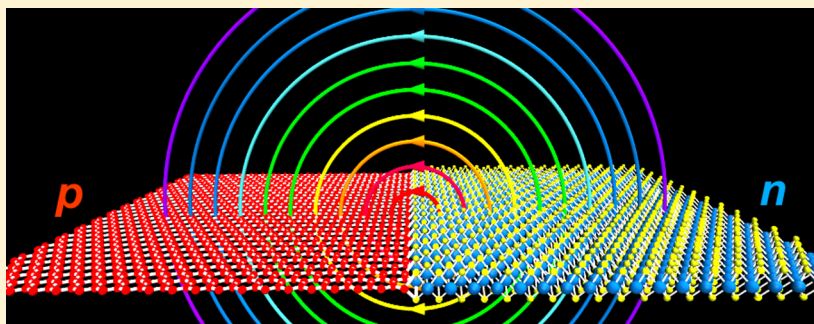


Carrier Delocalization in Two-Dimensional Coplanar p–n Junctions of Graphene and Metal Dichalcogenides

Henry Yu, Alex Kutana, and Boris I. Yakobson*

Department of Material Science and Nanoengineering, Department of Chemistry, and Applied Physics Program, Rice University, Houston, Texas 77005, United States

S Supporting Information



ABSTRACT: With the lateral coplanar heterojunctions of two-dimensional monolayer materials turning into reality, the quantitative understanding of their electronic, electrostatic, doping, and scaling properties becomes imperative. In contrast to traditional bulk 3D junctions where carrier equilibrium is reached through local charge redistribution, a highly nonlocalized charge transfer (trailing off as $1/x$ away from the interface) is present in lateral 2D junctions, increasing the junction size considerably. The depletion width scales as p^{-1} , while the differential capacitance varies very little with the doping level p . The properties of lateral 2D junctions are further quantified through numerical analysis of realistic materials, with graphene, MoS₂, and their hybrid serving as examples. Careful analysis of the built-in potential profile shows strong reduction of Fermi level pinning, suggesting better control of the barrier in 2D metal–semiconductor junctions.

KEYWORDS: Heterojunction, 2D material, Fermi level pinning, weak electronic screening, graphene, dichalcogenide

Two-dimensional materials have emerged as next key building blocks for nanotechnology, holding great promise for nanoelectronics. In order to exploit their remarkable properties in actual devices, 2D materials need to be interfaced with other systems, i.e., connected to electrodes or with each other. In this respect, 2D material heterojunctions are of great interest. While vertical heterostructures and junctions of graphene and other 2D materials have traditionally attracted most attention,^{1,2} recent experimental successes^{3–8} have put a spotlight on lateral, coplanar 2D junctions. For instance, a nearly perfect lateral graphene/h-BN junction has been recently made,³ and lateral junctions between two different 2D transition metal dichalcogenides have been realized.^{4,5} Electrically doped lateral graphene p–n junction made from a single graphene sheet utilizing the ambipolar field effect⁹ has also been reported.¹⁰ While ever-expanding availability and improving sample quality make experimental tests feasible, it also compels one to theoretically investigate properties of such lateral junctions in general and of specific heterostructures formed from typical 2D materials.

A tight contact of two materials in a heterojunction allows an exchange of carriers which equilibrates the Fermi levels, while also realigns the electronic bands. In a 3D junction the formed electric double layer is rather local but *planar*, making it

sufficient to create a global built-in potential step $\Delta\phi$, so that $\Delta E_F - \Delta\phi = 0$, where ΔE_F is the difference of the Fermi levels of the materials before contact (hereafter we use elementary charge e as a unit, so the energy and electrostatic potential have same dimensionality). The electric double layer consists of the highly localized dipoles, due to often-present interface states, and the region of width W fully depleted of carriers; there is also a transition region¹¹ between the space-charged depletion region and the neutral material away from the junction. In the 3D case the transition region is very narrow, which justifies the well-known abrupt depletion-layer approximation.^{11,12} In 2D lateral junction, the charge exchange forms a double layer which is not a plane, but merely a dipole line, whose electrostatic potential obviously decays with distance as $\sim x^{-1}$ and cannot build the global potential step $\Delta\phi$ needed for carrier equilibration.¹³ It means immediately that any interface chemical dipoles cannot cause 2D-junction band offset^{14,15} and the Fermi level pinning¹⁶ is suppressed. Less obvious, delocalized charge redistribution is necessary¹³ to form a global potential step $\Delta\phi$ equilibrating the Fermi level across the 2D

Received: May 4, 2016

Revised: June 17, 2016

Published: July 14, 2016

junction. Below we begin from the simplest heterojunction model of two metals with different work functions. It permits an analytical solution, clearly reveals the general trends in charge and potential behavior across the lateral 2D junctions, and determines the key differences from the bulk case. We then go on to explore in some detail selected 2D junctions of realistic materials (gapless semimetal graphene, semiconductor MoS₂, and their hybrid structure) using the semiclassical macroscopic model with its material-specific parameters drawn from the electronic structure density functional theory (DFT) calculations. In case of hybrid structure (e.g., Gr/MoS₂), the role of interface states and limitations of the Fermi level pinning in Schottky barrier behavior are discussed.

The important distinction between 3D and 2D junctions can be captured by the analysis of lateral heterojunction of two semi-infinite metal sheets; see Figure 1a. If the difference of the

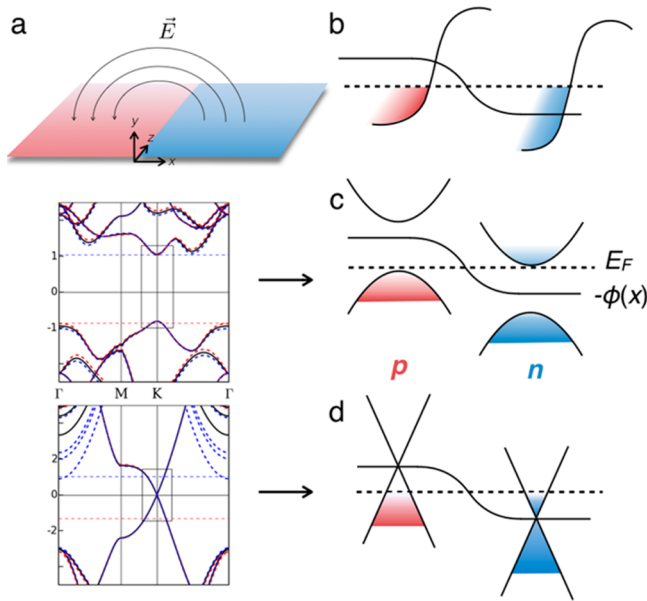


Figure 1. Schematics of a lateral coplanar 2D heterojunction (a) and (b–d) of band alignments in the contacts of two metals (b) and semiconductor (c) or graphene (d) p–n junctions. E_F is the equilibrated Fermi level, and $\phi(x)$ is the built-in potential within the plane of the materials. Full band structures of a 2D semiconductor (MoS₂) and graphene, with doping levels of -0.1 (red dashed), 0.0 (black solid), and $+0.1$ (blue dashed) $e/cell$ are shown on the left. Horizontal lines show positions of the Fermi level for each doping degree.

metal Fermi levels is $\Delta E_F = \Delta\phi$, the 2D Poisson equation for the potential distribution $\phi(x,y)$ is

$$\nabla^2\phi(x,y) = -4\pi\sigma(x)\delta(y) \quad (1)$$

with the boundary conditions $\phi(x = \pm\infty, y = 0) = \pm\Delta\phi/2$. Here x is the in-plane direction normal to the interface line z , y is the out-of-plane direction, and $\sigma(x)$ is the surface charge density, multiplied by $\delta(y)$ for a thin junction layer. Translational symmetry is assumed along z . We find that eq 1 is analytically tractable, with elegantly simple solution $\phi(x,y) = \Delta\phi/\pi \tan^{-1}(x/y)$. The in-plane surface charge density $\sigma(x)$ is therefore given by

$$\sigma(x) = -(1/\pi)\partial\phi/\partial y\Big|_{y=0} = 1/2(\Delta\phi/\pi^2)(1/x) \quad (2)$$

The charge density is proportional to the Fermi level difference $\Delta E_F = \Delta\phi$, and its singularity at the origin would be truncated by the carrier concentration in a real metal. Truncation of the singular dipole has only very localized effects and leads to interface region of small width W (see Supporting Information). The extensive tail $\sigma \sim 1/x$ is however a common feature of all lateral 2D heterojunctions. The necessity of the long charge tail in 2D junctions and even its functional form can be understood by estimating the integral of the electric field, $E(x) = 2\pi\sigma(x)$ at the surface $y = 0$ and then of nearly constant value over an arch-path connecting two remote points $\pm x$. The path length is πx , so that $2\pi^2\sigma(x) \cdot x = \Delta\phi$, which yields precisely eq 2. Note the diverging integral $\int_{-\infty}^{\infty}\sigma(x) dx$ where $W > 0$, indicating the extensive charge transfer in a 2D junction, limited in reality by the device size L at the upper limit.

We also note that eq 2 contains no length scale at all to characterize the width of the junction, unless a finite carrier density is introduced. The latter becomes essential when turning to p–n junction with carrier density limited by the dopant (areal) concentration $c = p/a^2$, p being probability of a dopant per unit cell of area a^2 . Accordingly the maximum carrier charge density is limited by $\sigma(x) \leq ec$. Combined with eq 2, one finds the width of depletion region as

$$W_2 = 1/2(\Delta\phi/\pi^2c) \sim \Delta\phi/p \quad (3)$$

Note that its scaling with the built-in potential and the dopant concentration is qualitatively different from that in a 3D junction, where $W_3 \sim (\Delta\phi/p)^{1/2}$.¹¹ Yet more striking difference is in the extensive transition region $\sigma(x) \sim 1/x$, generally negligible in 3D junctions. Now that significant new features of 2D junction are captured, we go on to explore how it will be affected by specific material details in case of p–n junction in real semiconductor (e.g., MoS₂) or semimetal (graphene, Gr) or possibly their heterojunction (Gr/MoS₂).

For materials with a moderate carrier density (semiconductor, semimetal), eq 1 is no longer sufficient to obtain the potential and charge density, requiring a more material-specific account. Using full atomistic description such as the DFT is impractical:¹⁷ as the above eqs 2–3 suggest and is shown below, depletion regions span very long range in 2D junctions, from 10 to 10⁴ nm which is orders of magnitude greater than in 3D; the standard plane wave basis used for extended systems imposes periodicity in all directions, requiring a supercell of at least 10² ~ 10⁸ nm³ size (see Supporting Information). Instead, we employ a more manageable semiclassical approach¹² by considering the following expression for the charge distribution $\sigma(x)$:

$$\sigma(x) = \sigma_+ + ec - \int_{-\infty}^{\Phi(x)} C_q d\phi' \quad (4)$$

Here, the local charge density $\sigma(x)$ is obtained by adding the constant positive background from the host material (σ_+) and dopant ion concentration ($c = p/a^2$). The important variable third term represents the electrons stored by the layer intrinsic (quantum) capacitance C_q charged up to the local voltage $\phi(x) \equiv \phi(x, y = 0)$. This quantum capacitance is directly related to the density of states available to the electrons, $D(\epsilon)$ or DOS.^{18,19} $C_q = \partial\sigma/\partial\phi = \int D(\epsilon)(-\partial f(\epsilon - \phi)/\partial\epsilon) d\epsilon$, where $f(\epsilon)$ is the Fermi function. This expression relies on a rigid band approximation (RBA) for the DOS, i.e., $D(\epsilon)$ independent of the local external potential $\phi(x)$ and charge $\sigma(x)$. To obtain the potential and charge distributions, eqs 1 and 4 are solved self-

consistently.²⁰ By choosing the appropriate harmonic basis for the 2D Poisson equation, we are able to consider an infinite box length in the y direction, which is essential to capture the long-ranged features in a 2D junction. The use of RBA for the DOS is justified, as is clear from Figure 1c–d, which show full band structures of MoS₂ and graphene charged to $p = -0.1$ (red), 0.0 (black), and +0.1 (blue). The band structures change very slightly with charging, showing almost rigid bands under doping of ± 0.1 . Actual typical dopant levels are much smaller, from 10^{-6} to 10^{-3} , where the RBA is valid *a fortiori*.

With these provisions we are ready to analyze two representative p–n junctions in monolayer semiconductors (MoS₂, Figure 1b) and semimetals (graphene, Figure 1c). Both junctions are assumed abrupt and having no interface states. For the p–n junction of MoS₂, the DOS near the band edges derives from the doubly degenerate parabolic bands originating from the K and K' valleys, with respective hole and electron masses of $m_h = 0.58 m$ and $m_e = 0.48 m$,^{21,22} m being the nominal electron mass; an experimental band gap of 1.85 eV²³ was assumed. The p- and n-dopant ion concentration of $p = 10^{-4}$ was used symmetrically for MoS₂, which results in a built-in potential of $\Delta\phi = 1.60$ V. To contrast the dimension-related behaviors more clearly, we also consider an equivalent hypothetical 3D semiconductor p–n junction with identical effective masses, band degeneracy, dopant concentration, and natural layer-spacing in the y -direction. Other choices for the parameters of 3D materials are possible; however, they do not alter the results significantly.

For the DOS of graphene near the Dirac point, a linear dispersion $D(E) = (2/\pi\hbar^2 v_F^2)|E|$ was used,²⁴ with $v_F = 10^6$ m/s Fermi velocity. A dopant ion concentration $p = 1.5 \times 10^{-4}$ was applied symmetrically, resulting in a built-in potential of $\Delta\phi = 0.093$ V. The corresponding 3D p–n junction had graphene DOS, and the natural interlayer spacing in y -direction is assumed. A temperature $T = 300$ K was used for the Fermi function in all calculations. The Fermi level of all materials is assumed to be controlled by the dopant type and amount, given by the dopant concentration p .

The calculated charge densities and electrostatic potentials are shown in Figure 2. Red solid curves plot solutions for 2D materials (MoS₂, graphene); red dashed curves are the asymptotic forms given by eq 2, and blue solid curves correspond to the 3D junctions.

The charge distribution in a coplanar MoS₂|MoS₂ p–n junction is shown in the top panel of Figure 2a with a solid red line. The fully depleted area with constant charge near the contact transitions into a long charge tail extending into the material, approaching the asymptote $\sim 1/x$ (dashed red line) as predicted by eq 2. The depletion width W , defined as a distance to the intersection of the full depletion level and perfect metal solution, is ~ 48 nm for this case. In contrast, the charge distribution in the corresponding 3D junction (solid blue line) drops rather abruptly at ~ 5 nm, without long tail. The potential profile in a MoS₂|MoS₂ p–n junction, shown in the bottom panel of Figure 2a with a solid red line, reaches the asymptotic value over the length of more than 60 nm. The potential varies rather slowly, change of $\Delta\phi/2 = 0.8$ V over 192 unit cells of MoS₂ amounts to 4 meV per unit cell. This contrasts with the potential in the bulk junction (solid blue line) reaching the asymptotic value at just ~ 4 nm.

The fully depleted region is absent in gapless graphene, and the charge density in Figure 2b decreases gradually, approaching $\sim 1/x$ behavior at ~ 10 nm. We define the width

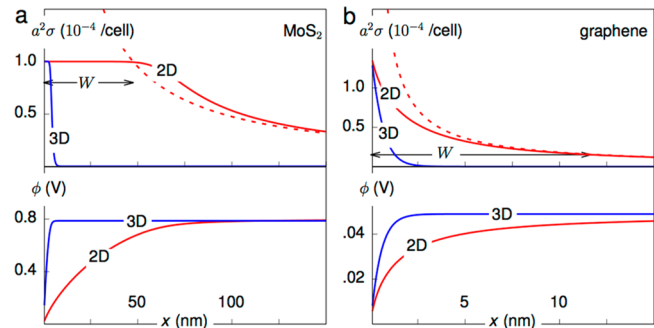


Figure 2. Computed electrostatic potential and surface charge density in 2D lateral MoS₂|MoS₂ and graphene|graphene p–n junctions; only the n -doped side is shown. (a) Surface charge density (top) and electrostatic potential (bottom) for symmetrically doped 2D (solid red lines) and 3D bulk (solid blue lines) MoS₂ p–n junctions with doping $p = 10^{-4}$. The asymptotic behavior of eq 2 is shown with a red dashed line; the depletion width $W = 48$ nm is marked. (b) Surface charge density (top) and electrostatic potential (bottom) for symmetrically doped lateral 2D and 3D bulk graphene p–n junctions with $p = 1.5 \times 10^{-4}$; width $W = 12$ nm of graphene junction is marked.

of graphene junction as W where $\sigma(W) = 0.1p/a^2$, which yields $W = 12$ nm. In contrast, the charge density for the corresponding 3D junction (solid blue line) drops rather quickly within 2 nm, without a long tail. The potential profile for Gr|Gr p–n junction (solid red line in the bottom of Figure 2b) approaches the asymptotic value at ~ 10 nm. This corresponds to the $\Delta\phi$ gradient of 1.1 meV per unit cell, small enough to justify using ϕ as a parameter in the RBA for this system. It is clear from Figure 2 that in both examples of MoS₂ and Gr the depletion widths of 2D junctions are much greater than those of 3D analogues. More importantly, an extensive charge transfer with a $1/x$ charge tail is present in 2D junctions, while in 3D the charge transfer is localized and drops rapidly to zero over a small distance.

These qualitative differences between the 2D and 3D junctions would be reflected in their response to the applied voltage. According to eq 3, the depletion widths scale as different powers of the built-in potential, $W \sim \Delta\phi^{1/(d-1)}$ with $d = 2$ or 3, for the 2D or 3D cases. When the forward bias V is applied, the potential step becomes $\Delta\phi - V$, allowing one to determine how the depletion width W depends on the bias voltage, using eq 3. The depletion width can be measured indirectly through differential capacitance of the junction. For traditional 3D junctions the differential capacitance is given by $C_{3D} \sim p^{1/2}(\Delta\phi - V)^{-1/2} \sim W_3^{-1}$.¹¹ The capacitance of a 2D junction has a different form. For a 2D junction of finite total length L with the total charge Q (per transverse length) the capacitance $C_{2D} = dQ/dV$ can be calculated using eqs 2–3 as $C_{2D} = (1/2\pi^2) \ln(L/W_2)$. This yields an exponential relation, $W_2 = L \exp(-2\pi^2 C_{2D})$, between the depletion width of a 2D junction and its measured capacitance. Figure 3 shows the computed W_2 for both junctions as a function of doping level p . The computed widths are plotted with red circles (for MoS₂) and red crosses (for Gr), with the corresponding predictions of eq 3 shown as thin lines. For a semiconductor like MoS₂, the built-in potential $\Delta\phi$ is mainly determined by the band gap, with only small change due to doping, i.e., $\Delta\phi \approx \text{const}$ and, according to eq 3, the depletion width changes as $\sim p^{-1}$, in close agreement with the computed data in Figure 3. In graphene, where DOS is decreasing near the Dirac point, the built-in potential depends strongly on the dopant concen-

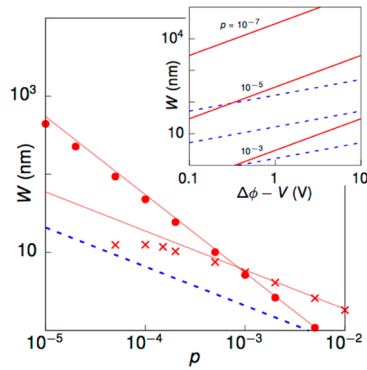


Figure 3. Depletion width W in $\text{MoS}_2|\text{MoS}_2$ and $\text{Gr}|\text{Gr}$ p-n junctions. Red circles show computed widths W_2 of lateral 2D MoS_2 junctions, and the red solid line is from eq 3; blue dashed line shows the depletion width W_3 of a corresponding 3D semiconductor. Red crosses and the tracking red line show similar results for graphene. The inset compares the depletion widths of 2D (red lines) and 3D (blue dashed lines) semiconductors as functions of the total built-in potential $\Delta\phi - V$; depletion widths W_2 for 2D (red lines) and the widths W_3 for the 3D analogue (blue dashed lines) are shown for $p = 10^{-7}$, 10^{-5} , and 10^{-3} .

tration. The relation between the built-in potential and doping can be expressed as $p = \int_0^{\Delta\phi/2} D(E) dE = (1/\pi\hbar^2 v_F^2) \Delta\phi^2$ if temperature is ignored, which gives $\Delta\phi \sim p^{1/2}$. Substituting into eq 3, we have $W_2^{\text{graphene}} \sim \Delta\phi/p \sim p^{-1/2}$, which is also in close agreement with computed values in Figure 3 for high doping ($p > 10^{-4}$). For low doping, the built-in potential $\Delta\phi$ for graphene becomes comparable to the thermal energy $k_B T = 26$ meV. In this region the carriers are created predominantly by thermal excitations, and the W reaches a plateau at $p < 10^{-4}$.

The difference in scaling with junction dimensionality is further illustrated by plotting the depletion width of eq 3 for a 2D $\text{MoS}_2|\text{MoS}_2$ p-n junction, at $p = 10^{-7}$, 10^{-5} , and 10^{-3} (solid red lines, Figure 3 inset). Depletion widths of the 3D p-n junctions are plotted as blue dashed lines. The standard formula $W_3 = [(\Delta\phi - V)/(2\pi^2 c)]^{1/2}$ for the bulk junction is used,¹¹ also at $p = 10^{-7}$, 10^{-5} , and 10^{-3} . Due to the difference in scaling laws, the slopes and vertical spacing for the 2D results are twice as those of the 3D, and the depletion widths of 2D junctions greatly exceed those of 3D. If we consider a typical case where $\Delta\phi - V = 1$ V, it is seen from the figure that a doping level of $p \sim 10^{-3}$ is needed to enter the 100 nm scale, and a value of p higher than 10^{-3} is required to enter the nanometer scale. This indicates that, in nanometer scale device applications, one should expect a fully depleted lateral 2D junction for any typical p values. Only when the semiconductor is doped as strongly as $p > 10^{-3}$ should one expect $W < L$. With embedding medium of dielectric constant $\epsilon > 1$, the length scale is expected to be even larger.

Finally, we turn to a heterojunction, where chemical disruption brings about the interfacial states, causing Fermi level pinning that notoriously affects the Schottky barrier in bulk metal–semiconductor devices.²⁵ How and if these effects are different in coplanar geometry can be explored within the same approach by accounting for the interfacial states, also participating in the charge equilibration process. The interfacial dipole in a 3D junction is planar and creates a global potential step throughout the junction, leading to the deviation from the Schottky–Mott rule for the barrier (and band alignment) of metal–semiconductor junctions.^{14–16} If the density of interfacial states is very large, the barrier height is dominated by the

interface and decouples from the metal work function, leading to possibly full Fermi level pinning.²⁶ In contrast, in 2D junction the interfacial dipole is linear and can only create local potential variation, vanishing at a distance; since interface state charging cannot affect band offset remotely, it may seem at a first glance that pinning is not possible at all.

In order to quantify the situation, we include an interfacial term into eq 4. The essential role of the interfacial states can be captured by their constant DOS, $D_i = n/E_g$ uniformly distributed within the band gap E_g of the semiconductor,²⁶ where n is the linear density of interfacial states at the contact. The resulting charge density σ_i accumulated at the interface is $\sigma_i = D_i(E_{\text{neu}} - \phi(0) - E_F) \cdot \delta(x)$. Here, E_{neu} is the neutrality level,¹⁶ and multiplication by $\delta(x)$ denotes a thin region at the interface. This term should be added into eq 4, solved self-consistently with eq 1 to obtain the potential and charge profile across the 2D Schottky junction. The solution naturally produces a countercharge on the metal side, resulting into an interfacial dipole. Here we select as example heterojunction of $\text{Gr}|\text{MoS}_2$,²⁷ where MoS_2 has electron affinity χ and is n-doped to $p = 10^{-4}$. Due to lattice mismatch, such interface must be of bad quality, containing strained and dangling bonds, which justifies considering broad range of interface state densities up to high values of n in our phenomenological model. To mimic the change of metal work function due to contact with different metals, we vary the work function ϕ_w of graphene and compute the resulting Schottky barrier height ϕ_B . The results are shown in Figure 4 for $n = 0$, 10^{-3} , and 10^{-2} . The ideal case of the

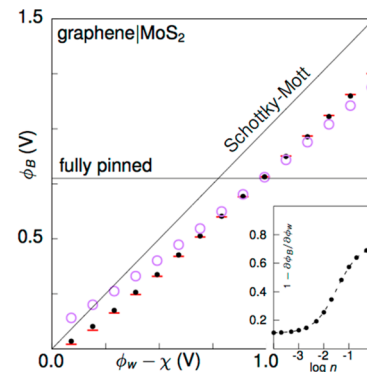


Figure 4. Computed Schottky barrier height ϕ_B as a function of $\phi_w - \chi$, the difference between the metal workfunction and electron affinity of the semiconductor. Red dashes, solid black dots, and empty purple circles are results for densities of interfacial states $n = 0$, 10^{-3} , and 10^{-2} , respectively. Black straight lines show the fully pinned and Schottky–Mott limits. Inset shows the calculated pinning strength $1 - \partial\phi_B/\partial\phi_w$ as a function of the interfacial states density n .

Schottky–Mott rule and the fully pinned limit are shown as thin lines. Although the slopes vary not far from unity, it is clear that the interface dipole does have local effect, sufficient to reduce the barrier and cause some degree of Fermi level pinning (in contrast to band offset which cannot be pinned at all by a localized linear dipole potential; see also Supporting Information). The inset in Figure 4 shows the pinning strength $S \equiv 1 - \partial\phi_B/\partial\phi_w$ as a function of the density of interfacial states n . Note that the pinning strength never reaches the fully pinned limit $S = 1$, instead remaining near one-half even at very high interfacial state concentrations, in accord with qualitative assessment above.

In summary, we studied the charge equilibration processes in 2D lateral heterojunctions. The calculations predict an extensive charge transfer across the interface, due to the reduced electronic screening in 2D systems. A universal trait of $\sim 1/x$ for the charge density decreasing slowly away from the interface, and scaling rule for the depletion region width $W \sim \Delta\phi/p$ (with the built-in potential $\Delta\phi$ and doping level p) are established. In particular, instead of a very narrow transition region between the depleted and neutral zones in the 3D case, here the transition region dominates and may span the entire device. We thus find that the 2D Schottky devices may have a much greater length scale compared to bulk junctions or can be otherwise fully depleted and tuned by the size itself. The extensive depletion region should reduce leakage current and thus improve the device on/off ratio. The electric field across large area of space charge may assist charge separation in photovoltaic applications, provided the electron–hole attraction is weak, so that reduced field strength is not too detrimental. Finally, the well-known issue of Fermi level pinning in a Schottky junction appears less significant in 2D systems, allowing a much better control of the Schottky barrier height with respect to the change of the metal work function.

■ ASSOCIATED CONTENT

📄 Supporting Information

The Supporting Information is available free of charge on the ACS Publications website at DOI: [10.1021/acs.nanolett.6b01822](https://doi.org/10.1021/acs.nanolett.6b01822).

Model validation, electrostatic solution for periodic systems, DFT calculation of interface dipole in a graphene/BN system, potential profile in the presence of Fermi level pinning (PDF)

■ AUTHOR INFORMATION

Notes

The authors declare no competing financial interest.

■ ACKNOWLEDGMENTS

This work was supported by the Office of Naval Research grant N00014-15-1-2372.

■ REFERENCES

- (1) Geim, A. K.; Grigorieva, I. V. *Nature* **2013**, *499* (7459), 419–425.
- (2) Liu, Y.; Stradins, P.; Wei, S.-H. *Sci. Adv.* **2016**, *2* (4), e1600069.
- (3) Liu, L.; Park, J.; Siegel, D. A.; McCarty, K. F.; Clark, K. W.; Deng, W.; Basile, L.; Idrobo, J. C.; Li, A.-P.; Gu, G. *Science* **2014**, *343* (6167), 163–167.
- (4) Huang, C.; Wu, S.; Sanchez, A. M.; Peters, J. J. P.; Beanland, R.; Ross, J. S.; Rivera, P.; Yao, W.; Cobden, D. H.; Xu, X. *Nat. Mater.* **2014**, *13*, 1096–1101.
- (5) Gong, Y.; Lin, J.; Wang, X.; Shi, G.; Lei, S.; Lin, Z.; Zou, X.; Ye, G.; Vajtai, R.; Yakobson, B. I.; Terrones, H.; Terrones, M.; Tay, B. K.; Lou, J.; Pantelides, S. T.; Liu, Z.; Zhou, W.; Ajayan, P. M. *Nat. Mater.* **2014**, *13* (12), 1135–1142.
- (6) Worne, J. H.; Giridharagopal, R.; Kelly, K. F.; Natelson, D. *Nano Res.* **2008**, *1* (4), 341–350.
- (7) Worne, J. H.; Gullapalli, H.; Galande, C.; Ajayan, P. M.; Natelson, D. *Appl. Phys. Lett.* **2012**, *100* (2), 23306.
- (8) He, Y.; Sobhani, A.; Lei, S.; Zhang, Z.; Gong, Y.; Jin, Z.; Zhou, W.; Yang, Y.; Zhang, Y.; Wang, X.; Yakobson, B.; Vajtai, R.; Halas, N. J.; Li, B.; Xie, E.; Ajayan, P. *Adv. Mater.* **2016**, <http://dx.doi.org/10.1002/adma.201600278>.
- (9) Novoselov, K. S.; Geim, A. K.; Morozov, S. V.; Jiang, D.; Katsnelson, M. I.; Grigorieva, I. V.; Dubonos, S. V.; Firsov, A. A. *Nature* **2005**, *438* (7065), 197–200.
- (10) Williams, J. R.; DiCarlo, L.; Marcus, C. M. *Science* **2007**, *317* (5838), 638–641.
- (11) Sze, S. M. *Physics of semiconductor devices*, 3rd ed.; Wiley-Interscience: Hoboken, NJ, 2007.
- (12) Ashcroft, N. W.; Mermin, N. D. *Solid State Physics*; Saunders College Publishing, 1976.
- (13) Yu, H.; Kutana, A.; Yakobson, B. I. In *APS March Meeting Abstracts*; 2015; <http://meetings.aps.org/Meeting/MAR15/Session/W2.3>.
- (14) Baldereschi, A.; Baroni, S.; Resta, R. *Phys. Rev. Lett.* **1988**, *61* (6), 734–737.
- (15) Tersoff, J. *Phys. Rev. B: Condens. Matter Mater. Phys.* **1984**, *30* (8), 4874–4877.
- (16) Tung, R. T. *Appl. Phys. Rev.* **2014**, *1* (1), 11304.
- (17) Tian, X.; Liu, L.; Du, Y.; Gu, J.; Xu, J.; Yakobson, B. I. *Phys. Chem. Chem. Phys.* **2015**, *17*, 31685–31692.
- (18) Luryi, S. *Appl. Phys. Lett.* **1988**, *52* (6), 501–503.
- (19) Rahman, A.; Guo, J.; Datta, S.; Lundstrom, M. S. *IEEE Trans. Electron Devices* **2003**, *50* (9), 1853–1864.
- (20) Léonard, F.; Tersoff, J. *Phys. Rev. Lett.* **1999**, *83* (24), 5174–5177.
- (21) Shi, H.; Pan, H.; Zhang, Y.-W.; Yakobson, B. *Phys. Rev. B: Condens. Matter Mater. Phys.* **2013**, *87* (15), 155304.
- (22) Kutana, A.; Penev, E. S.; Yakobson, B. I. *Nanoscale* **2014**, *6* (11), 5820–5825.
- (23) Liu, H.; Antwi, K. K. A.; Chua, S.; Chi, D. *Nanoscale* **2014**, *6* (1), 624.
- (24) Castro Neto, A. H.; Guinea, F.; Peres, N. M. R.; Novoselov, K. S.; Geim, A. K. *Rev. Mod. Phys.* **2009**, *81* (1), 109–162.
- (25) Tung, R. T. *Phys. Rev. Lett.* **2000**, *84* (26), 6078–6081.
- (26) Bardeen, J. *Phys. Rev.* **1947**, *71* (10), 717–727.
- (27) Ling, X.; Lin, Y.; Ma, Q.; Wang, Z.; Song, Y.; Yu, L.; Huang, S.; Fang, W.; Zhang, X.; Hsu, A. L.; Bie, Y.; Lee, Y.-H.; Zhu, Y.; Wu, L.; Li, J.; Jarillo-Herrero, P.; Dresselhaus, M.; Palacios, T.; Kong, J. *Adv. Mater.* **2016**, *28* (12), 2322–2329.